

Analysis and Design of Commutation-Based Circulator-receivers for Integrated Full-Duplex Wireless

Negar Reiskarimian^{ID}, *Student Member, IEEE*, Mahmood Baraani Dastjerdi, *Student Member, IEEE*,

Jin Zhou, *Member, IEEE*, and Harish Krishnaswamy^{ID}, *Member, IEEE*

Abstract—Previously, we presented a non-magnetic, non-reciprocal N-path-filter-based circulator-receiver (circ.-RX) architecture for single-frequency full-duplex (SF-FD) wireless, which merges a commutation-based linear periodically time-varying (LPTV) non-magnetic circulator with a down-converting mixer and directly provides the baseband (BB) RX signals at its output, while suppressing the noise contribution of one set of the commutating switches. The architecture also incorporates an on-chip balance network to enhance the transmitter (TX)-RX isolation. In this paper, we present a detailed analysis of the architecture, including a noise analysis and an analysis of the effect of the balance network. The analyses are verified by the simulation and measurement results of a 65-nm CMOS 750-MHz circ.-RX prototype. The circ.-RX can handle up to +8 dBm of TX power with 8-dB noise figure (NF) and 40-dB average isolation over 20-MHz radio frequency (RF) bandwidth (BW). In conjunction with digital self-interference (SI) and its third-order intermodulation (IM3) cancellation, the SF-FD circ.-RX demonstrates 80-dB overall SI suppression for up to +8-dBm TX average output power. The claims are also verified through an SF-FD demonstration where a -50-dBm weak desired received signal is recovered while transmitting a 0-dBm average power orthogonal frequency-division multiplexing (OFDM)-like TX signal.

Index Terms—Circulator, CMOS, full-duplex (FD) wireless, interference cancellation (IC), non-reciprocity.

I. INTRODUCTION

THE thousandfold data capacity increase envisioned in the next generation of wireless communication networks or “5G” is expected to be delivered by technology candidates such as single-frequency full-duplex (SF-FD) wireless and massive multiple-input multiple-output (MIMO) wireless [1], [2]. FD aims to instantly double the link capacity in the physical layer by simultaneously transmitting and receiving at the same frequency, as well as providing other

Manuscript received January 22, 2018; revised April 9, 2018; accepted April 12, 2018. Date of publication May 22, 2018; date of current version July 20, 2018. This paper was approved by Associate Editor Pietro Andreani. This work was supported in part by the Defense Advanced Research Projects Agency ACT Program, in part by the NSF EFRI Program, and in part by a Qualcomm Innovation Fellowship. (*Corresponding author: Harish Krishnaswamy*)

N. Reiskarimian, M. B. Dastjerdi, and H. Krishnaswamy are with the Department of Electrical Engineering, Columbia University, New York, NY 10027 USA (e-mail: harish@ee.columbia.edu).

J. Zhou is with the Department of Electrical and Computer Engineering, University of Illinois at Urbana-Champaign, Urbana, IL 61801 USA.

Color versions of one or more of the figures in this paper are available online at <http://ieeexplore.ieee.org>.

Digital Object Identifier 10.1109/JSSC.2018.2828827

benefits in the higher layers such as better spectral efficiency, reducing network and feedback signaling delays, and resolving hidden-node problems to avoid collisions [3]–[6].

Achieving the $2\times$ throughput gain and the other above-mentioned benefits is contingent upon overcoming several fundamental challenges associated with the FD operation. The first is the tremendous amount of self-interference (SI) from the transmitter (TX) at its own receiver (RX). An FD system handling +8 dBm of transmit power with 20-MHz signal bandwidth (BW) and 8-dB noise figure (NF) budget, requires almost 100 dB of SI cancellation (SIC) to cancel the TX leakage down to the RX noise floor of -93 dBm. This can only be achieved through multi-domain SIC at the antenna interface [7]–[13], radio frequency (RF)/analog baseband (BB) [8], [12], [14]–[20], and in digital [3], [8].

The second challenge is the implementation of fully-integrated single-antenna interfaces which can support simultaneous transmission and reception, while achieving low loss, low noise, high linearity, especially for TX-side excitations, and high isolation between the TX and the RX. Single-antenna FD is important to enable FD capability in hand-held devices [21], as well as extending it to MIMO applications, such as FD massive MIMO base stations to reduce the overhead of channel state information (CSI) estimation [22]. Previously reported single-antenna FD interfaces either use reciprocal electrical-balance duplexers [9]–[11], magnetic circulators [23] or non-reciprocal active quasi-circulators [17], [24]. Reciprocal antenna interfaces suffer from a fundamental minimum of 3-dB loss in the TX-antenna (ANT) and ANT-RX paths. In electrical-balance duplexers, the losses can be made asymmetric to favor either TX-ANT or RX NF performance [25]. Ferrite circulators require the use of magnetic materials which renders them incompatible with CMOS fabrication, and therefore bulky and expensive. Active quasi-circulators are limited by the noise and linearity performance of the active devices.

Reciprocity can be broken using temporal modulation, a fact recognized decades ago in the microwave community [26], [27]. More recently, there has been work on non-magnetic passive non-reciprocal circulators based on spatio-temporal modulation of material properties such as permittivity [28]–[30] and conductivity [7], [31]–[33]. These approaches are promising since they can theoretically achieve low loss, low noise, and high isolation, and can be config-

ured to maximize linearity for TX-side excitations as we have shown before in [7], [8], and [34]. However, the practical demonstrations of these exciting but nascent approaches currently remain limited in performance, particularly in noise and TX power handling.

In [7], [8], and [34], non-reciprocity is achieved through phase-shifted commutation across a capacitor bank, i.e., within an N-path filter for low-loss small-form-factor RF applications. Furthermore, sub-harmonic commutation across transmission lines has been demonstrated to scale this concept to the millimeter-wave regime [31], as well as to RF applications with stringent watt-level TX power handling requirements [35].

In [36], we introduced a new FD RX architecture, namely an N-path-filter-based circulator-RX (circ.-RX), which re-purposes the commutation-based non-reciprocal circulator to also perform down-conversion and provides direct access to BB signals at its output, while maintaining noise performance that is comparable to mixer-first RXs [17], [37]. The resulting circ.-RX architecture has a low power consumption and NF since the antenna interface and mixing functionalities are achieved within the same block, eliminating the additional low-noise amplifier (LNA)/low-noise transimpedance amplifier (LNTA) and mixer and their sources of noise. It also has the additional benefits of allowing the co-design of the antenna interface and the RX, and the embedding of TX-RX isolation-enhancing techniques. The enhancement of TX-RX isolation through the embedding of a reconfigurable balance network increases TX power handling, as the TX swing across the N-path switches is reduced, and more isolation is achieved before the first active BB amplifier.

This paper expands on [36] by providing additional information on system requirements and circ.-RX evolution in Section II, analyses to quantify the noise performance, effect of the embedded balance network, and the tradeoff between linearity to TX excitations, isolation/balancing range, and TX-ANT/ANT-RX insertion loss in Section III, implementation details of the 65-nm CMOS 0.6–0.9-GHz circ.-RX in Section IV, and a description of the measurement results and an FD demonstration in Sections V and VI. Finally, Section VII concludes the paper.

II. FD SYSTEM REQUIREMENTS AND CIRCULATOR-RECEIVER EVOLUTION

As mentioned earlier, we have shown that linear periodically time-varying (LPTV) circuits such as N-path filters enable the achievement of passive non-reciprocity without the use of magnetic materials, and the integration of circulators in CMOS [7], [8]. This opens new opportunities for the design of fully-integrated FD transceivers where the transceiver is co-designed with the antenna interface. In this section, we define the FD link requirements and discuss some of the interesting features of an FD system where the antenna interface and FD RX are co-designed and co-optimized as a whole.

A. FD Link Requirements

Consider an FD system with a TX average output power of +8 dBm, signal BW of 20 MHz and NF budget of 8 dB.

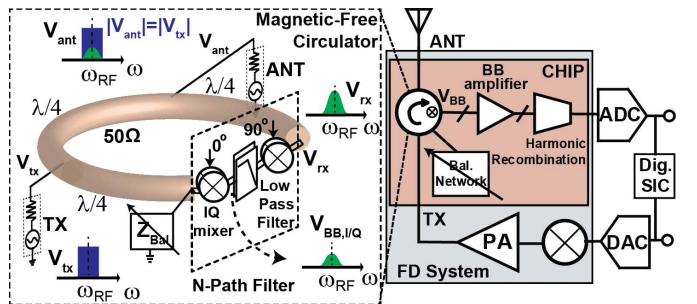


Fig. 1. FD N-path-filter-based circ.-RX conceptual architecture and block diagram.

The equivalent half-duplex noise floor is -93 dBm, requiring >100 -dB SIC. Our current system, shown in Fig. 1, is capable of providing about $+80$ dB of SIC across the antenna and digital domains, as is discussed later in Section V. In addition, we have previously reported in [8], the feasibility of BB SIC which can provide an additional 20 -dB cancellation.

Assuming a required SNR of 15 dB, 2.5-dBi TX, and RX dipole antenna gain, implementation losses of 5 dB, 10-dB margin for signal fading, and 5-dB ($3\times$) sensitivity degradation due to the residual SI and its third-order intermodulation (IM3), the link budget of $8 \text{ dBm} + 5 \text{ dBi} - (-93 \text{ dBm} + 5 \text{ dB} + 15 \text{ dB}) - 5 \text{ dB} - 10 \text{ dB} = 71 \text{ dB}$ translates to a transmission distance of 100 m at a frequency of 750 MHz (similar to the calculation done in [8]), which begins to approach the requirements for small-cell FD communication.

Detailed discussions of linearity requirements for such FD transceivers have been presented previously in [8]. A higher circulator isolation relaxes both the analog-to-digital converter (ADC) dynamic range and the SI-canceling RX effective 3rd order Input Intercept Point (IIP3). In addition, in our circulator architecture, increasing the isolation from TX to RX translates to lower voltage swings on the switches of the non-reciprocal element, which enhances the circulator linearity and the TX power handling as well.

B. RX Matching in Non-Reciprocal Antenna Interfaces

Integrated RXs are typically designed to have a $50\text{-}\Omega$ input impedance to provide matching for the conventional reciprocal antenna interfaces that precede them, such as surface acoustic wave (SAW) duplexers and filters. Matching is necessary to obtain the best filtering performance from the duplexer or filter. In addition, any mismatch at the RX port causes a reflection which travels back to the antenna due to reciprocity and causes undesired ANT re-radiation [Fig. 2(a) and (b)]. The need to simultaneously achieve input matching to $50\text{ }\Omega$ and noise matching for low noise performance, particularly over wide BWs, is the fundamental challenge of LNA/LNTA design.

Our FD RX in [8] followed a similar conventional design methodology, where the integrated circulator and the subsequent RX were both designed to provide a $50\text{-}\Omega$ impedance at the RX port. However, in the case of non-reciprocal antenna interfaces such as circulators, the RX reflection circulates away from the ANT and is absorbed at the TX port [Fig. 2(c) and (d)]. Hence, the Z_{rx} value shown in Fig. 2(d) does not need to be $50\text{ }\Omega$. It can be shown that increasing

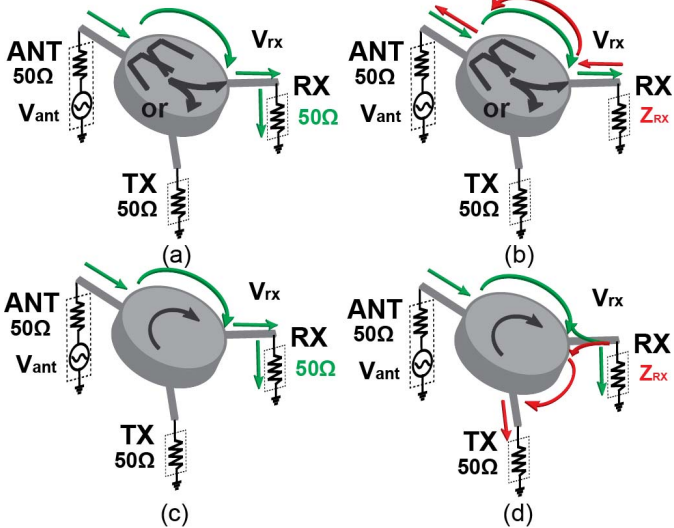


Fig. 2. Reciprocal antenna interface (a) matched at the RX port and (b) unmatched at the RX port where RX reflection returns to the ANT port. A non-reciprocal antenna interface (a) matched at the RX port and (b) unmatched at the RX port but preserving ANT matching.

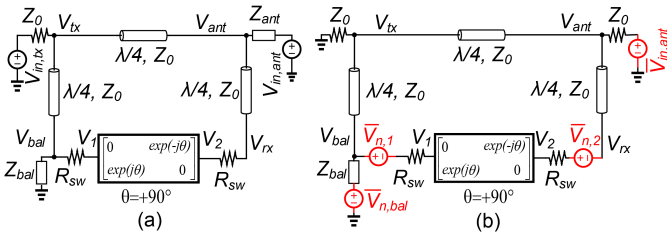


Fig. 3. Simplified model to analyze the effect of balance impedance on the performance of the circulator using the analytical S-parameters of the N-path filter (for $N \rightarrow \infty$) and series switch resistances for (a) TX and ANT excitations and (b) noise.

Z_{rx} increases the voltage gain from the ANT to the RX, and for the case of a high impedance RX interface ($Z_{rx} \rightarrow \infty$), the voltage gain is maximized to 6 dB for an ideal circulator

$$|V_{rx}| = \left| \frac{2V_{ant}}{1 + \frac{50}{Z_{rx}}} \right|, \text{ for } Z_{rx} \rightarrow \infty : |V_{rx}| = |2V_{ant}|. \quad (1)$$

It should be noted that after removing the RX termination, matching at the antenna port will depend on the TX port impedance (Z_{PA}) as shown in (2). This equation has been derived for the model in Fig. 3(a) (including the balancing impedance). In practice, other losses in the circulator, such as passive losses, will further improve the return loss seen at the ANT port

$$Z_{in,ant} = \frac{Z_{PA}}{1 + \frac{2Z_{PA}R_{SW}}{Z_0^2}}. \quad (2)$$

C. Embedded Down-Conversion and Noise Circulation

A conceptual architecture and block diagram of the circ.-RX are presented in Fig. 1. The circulator consists of a non-reciprocal LPTV gyrator built using an N-path filter [38], combined with three transmission line sections of an overall length of $3\lambda/4$ at the operation frequency [7], [8]. As with all N-path filters, the non-reciprocal element can also be viewed as a mixer low-pass filter (LPF)-mixer structure with phase-shifted clocks. In such a structure, it can be seen intuitively that

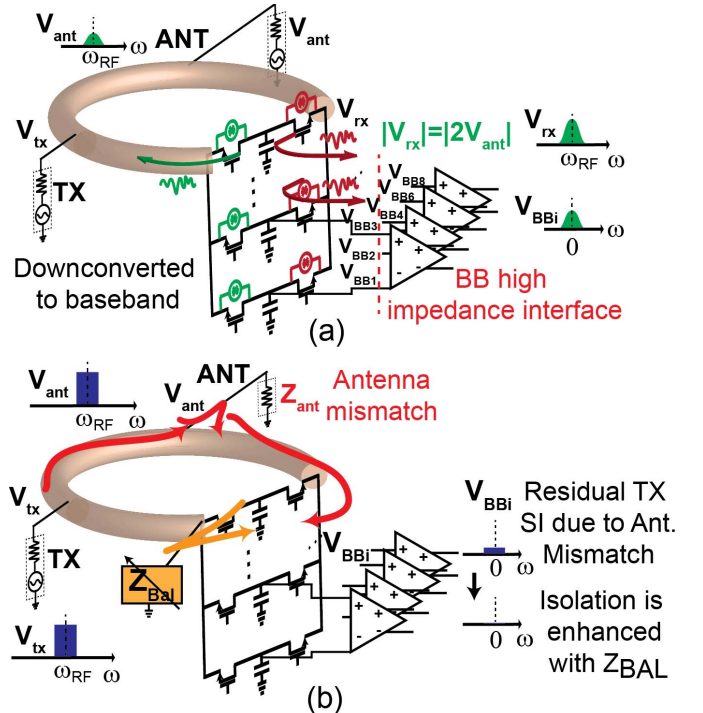


Fig. 4. Circ.-RX features (a) noise circulation and (b) isolation enhancement through a balance network that tracks antenna variations.

any RF signal appearing on Z_{rx} is down-converted and low-pass filtered by the BB capacitors. In other words, the circulator structure inherently includes a mixer-first RX, and the BB signals captured on the BB capacitors can be used for further BB processing. Importantly, isolation continues to be seen between the TX port and the N-path filter BB nodes.

Recall that in a passive non-return-to-zero (NRZ) mixer, we have [39]

$$\frac{I_{BB,1-path}}{I_{RF,in}} = \frac{2 \sin(\pi D)}{\pi} \frac{2D}{2D} \quad (3)$$

where $I_{BB,1-path}$ and $I_{RF,in}$ are the currents flowing into one of the BB paths and from the RF source, respectively. As an example, for an eight-path NRZ mixer with $D = 12.5\%$, $(I_{BB1-path}/I_{RF,in}) = -0.22$ dB, compared to $20\log(2/\pi) = -3.92$ dB in a two-path mixer. In other words, similar to the case of the NRZ mixer, by having a higher number of paths in the N-path filter, N , with lower duty cycle, $D = 1/N$, the RF-to-IF loss is improved since the fundamental component of the Fourier series for each local oscillator (LO) waveform is stronger. Subsequent recombination of different phases to create the In-phase/Quadrature (I/Q) signal can provide an effective RF-to-IF voltage gain. For example, combining the eight phases for the 3rd and the 5th harmonic rejection with $\pm 1, \pm(1/\sqrt{2}), 0, \mp(1/\sqrt{2})$ weights for $0^\circ/180^\circ, 45^\circ/225^\circ, 90^\circ/270^\circ$, and $135^\circ/315^\circ$ phases results in an additional 12-dB recombination voltage gain.

An additional interesting behavior in the circ.-RX is noise circulation. As we will show in Section III, the noise of the RX-side switches contribute mainly to the RX NF while the noise of the TX-side switches circulates away. Hence, the NF of the circ.-RX is theoretically as low as that of traditional mixer-first RXs despite the additional set of switches

[Fig. 4(a)]. It should also be noted that, while at higher frequencies, a mixer-first RX's performance is limited by the balance between R_{sw} of the mixers switches and the parasitic capacitance on the switch RF ports [40], in a circ.-RX, there is a possibility of absorbing the parasitic capacitors into the transmission line to extend the frequency limit [31]. However, a formal analysis of this is beyond the scope of this paper.

D. Enhancing Circulator Isolation

The TX-to-RX isolation in any three-port shared-antenna interface is limited to the quality of matching at the antenna port. In a practical system, antenna matching depends heavily on environmental reflections. As a result, antenna tuners are necessary to maintain TX-to-RX isolation across ANT variations. If placed at the antenna port, the tuner should be as linear as the antenna interface itself for the TX signals. In addition, parasitics within the circulator itself can limit the isolation achieved. Inspired by the concept of the balance network in electrical-balance duplexers [10], we have found that incorporating a tunable impedance on the TX side of the N-path filter, as shown in Fig. 4(b), can enhance TX-RX isolation. In essence, the tunable impedance creates a reflection that cancels out the reflected TX signal leaking to the BB nodes. It is also notable that in this paper, the balance network is placed at a low-voltage swing node with respect to the TX, hence maintaining the linearity benefits of the circulator. However, there exists a tradeoff between linearity, isolation, and loss, as will be discussed in Section III. In this paper, we have prioritized linearity and the TX power handling, and therefore the balance network is mainly effective in combating the effect of circuit parasitics, rather than handling large ANT variations.

III. ANALYSIS OF INTEGRATED COMMUTATION-BASED CIRCULATOR-RECEIVER PERFORMANCE METRICS

A. Effect of the Balance Network

In [8], we demonstrated a simplified method of analyzing the N-path-filter-based circulator, by using the fundamental-to-fundamental S-parameters of the N-path filter as a simplified model (ignoring harmonic conversion effects) along with the conventional microwave circuit analysis techniques for the overall structure. Using the same method, a simplified model for analyzing the circ.-RX in the presence of the balance network is shown in Fig. 3(a). The N-path filter is modeled using an ideal gyrator (assuming a large number of paths N) and the effect of switch resistance is captured through two series resistances with the gyrator element.

For an excitation at the TX, $V_{in,tx}$ in Fig. 3, the voltages at various nodes within the circulator can be found as

$$V_{ant} = -j V_{in,tx} \frac{Z_0}{R_{sw}} \frac{1}{2 + \frac{Z_0}{R_{sw}} \left(1 + \frac{Z_0}{Z_{ant}} \right)} \quad (4)$$

$$V_{bal} = -j V_{in,tx} \frac{2 + \frac{Z_0}{R_{sw}} \left(\frac{Z_0}{Z_{ant}} - 1 \right)}{\left(1 + \frac{Z_0}{Z_{bal}} \right) \left(2 + \frac{Z_0}{R_{sw}} \left(1 + \frac{Z_0}{Z_{ant}} \right) \right)} \quad (5)$$

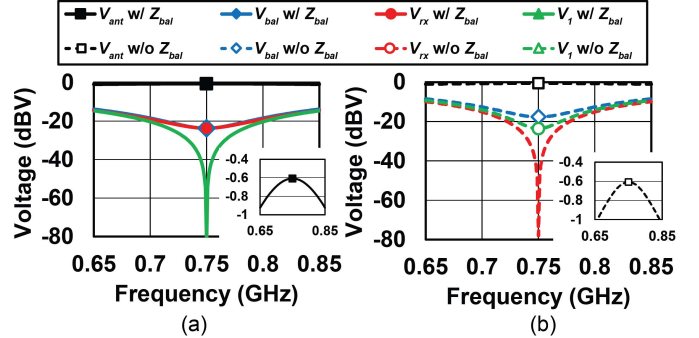


Fig. 5. Analysis and simulation results of the ideal circ.-RX shown in Fig. 3(a). (a) Without and (b) with the balance network across frequency for $V_{in,tx} = 2$ V. The analysis is shown with markers while the lines represent simulations across frequency. $Z_{ant} = 50$ Ω , $R_{sw} = 3.5$ Ω , and $Z_{ant} = 50$ Ω .

$$V_1 = -j V_2 = -j V_{in,tx} \frac{1 - \frac{Z_0}{Z_{bal}} + \frac{Z_0}{R_{sw}} \left(\frac{Z_0}{Z_{ant}} - 1 \right)}{\left(1 + \frac{Z_0}{Z_{bal}} \right) \left(2 + \frac{Z_0}{R_{sw}} \left(1 + \frac{Z_0}{Z_{ant}} \right) \right)} \quad (6)$$

$$V_{rx} = V_{in,tx} \frac{-\frac{2Z_0}{Z_{bal}} + \frac{Z_0}{R_{sw}} \left(\frac{Z_0}{Z_{ant}} - 1 \right)}{\left(1 + \frac{Z_0}{Z_{bal}} \right) \left(2 + \frac{Z_0}{R_{sw}} \left(1 + \frac{Z_0}{Z_{ant}} \right) \right)} \quad (7)$$

where V_{ant} is the voltage at the antenna port, V_{rx} and V_{bal} are the voltages at the right and left sides of the simplified non-reciprocal N-path filter in Fig. 3(a), and V_1 and V_2 are the voltages at the ideal gyrator ports (essentially the BB nodes, but without the frequency translation effect). This analysis in its current form is only valid at the center frequency of operation. However, an approach similar to [8] can be used to model the variation of the transmission lines' response across frequency, as well as that of the N-path filter. Due to the complexity of the equations, here we opted to limit the analysis to the center frequency and use Cadence Periodic Steady State (PSS)+Periodic Alternating Current (PAC) simulations to verify our results and show the performance across frequency.

From (6), by setting V_1 to 0, a formula for the desired Z_{bal} can be derived which nulls the TX leakage at the gyrator as follows:

$$Z_{bal} = \frac{Z_0 R_{sw} Z_{ant}}{R_{sw} Z_{ant} + Z_0 (Z_0 - Z_{ant})}. \quad (8)$$

Various important points can be deduced from the above-mentioned equations. First, Z_{bal} becomes 0 when R_{sw} is 0. This is representative of the fact that when R_{sw} is 0, the gyrator is ideal, which means that if balancing has been accomplished and V_1 is 0, then V_{bal} is 0 as well. This would render a shunt impedance at V_{bal} ineffectual. *Therefore, while placing the balancing impedance at V_{bal} leads to linearity benefits due to the low swing at that node for TX excitations, it limits the utility of the balancing impedance to the compensation of parasitics within the circulator and minor ANT impedance variations.* For $R_{sw} \neq 0$, for $Z_{ant} = 50$ Ω , the required Z_{bal} that results in perfect isolation is also 50 Ω . Fig. 5 shows the results of our analysis at the center frequency as well as simulations across frequency using Cadence for the ideal circuit analyzed earlier without the balance network and with the addition of the balance network for an excitation at

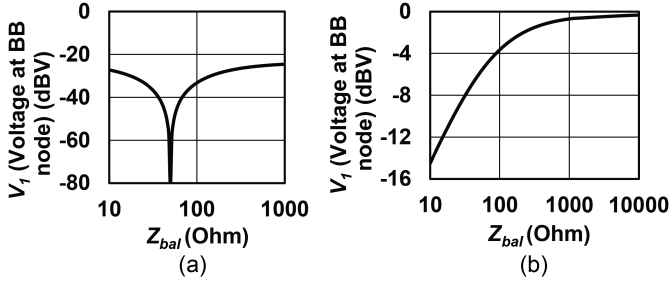


Fig. 6. Analysis of the effect of balance network on the ideal circ.-RX: gyrator voltage V_1 , representing the BB nodes, as a function of the balance resistance for (a) $V_{\text{in,tx}} = 2\text{-V}$ TX excitation in Fig. 3(a) ($V_{\text{in,ant}} = 0\text{ V}$) and (b) $V_{\text{in,ant}} = 2\text{-V}$ ANT excitation in Fig. 3(a) ($V_{\text{in,tx}} = 0\text{ V}$). $Z_{\text{ant}} = 50\Omega$ and $R_{\text{sw}} = 3.5\Omega$.

the TX port. As can be seen, without the balance network, in the presence of finite R_{sw} , perfect isolation is seen at V_{rx} but there is finite voltage swing at V_1 and V_{BAL} . However, by tuning the balance network according to (8) (i.e., to 50Ω), the TX leakage is canceled at the gyrator node V_1 . Second, the TX-to-ANT loss in this case is largely not affected by the balance impedance Z_{bal} , and only depends on the R_{sw} and Z_{ant} . This is another expected benefit of placing the balancing impedance at a node which has low swing for TX signals. Third, as an example after balancing, V_{bal} is -23 dB below V_{tx} for $R_{\text{sw}} = 3.5\Omega$ and $Z_{\text{ant}} = 50\Omega$, indicating the extent to which the power handling requirements on the balance network are relaxed.

Similarly, for an excitation at the ANT port, $V_{\text{in,ant}}$, the various voltages are

$$V_1 = -jV_2 = -2V_{\text{in,ant}} \frac{\frac{Z_0}{Z_{\text{ant}}} \left(\frac{Z_0}{R_{\text{sw}}} + \frac{1}{2} \left(1 + \frac{Z_0}{Z_{\text{bal}}} \right) \right)}{\left(1 + \frac{Z_0}{Z_{\text{bal}}} \right) \left(2 + \frac{Z_0}{R_{\text{sw}}} \left(1 + \frac{Z_0}{Z_{\text{ant}}} \right) \right)} \quad (9)$$

$$V_{\text{bal}} = -2V_{\text{in,ant}} \frac{\frac{Z_0}{Z_{\text{ant}}} \frac{Z_0}{R_{\text{sw}}}}{\left(1 + \frac{Z_0}{Z_{\text{bal}}} \right) \left(2 + \frac{Z_0}{R_{\text{sw}}} \left(1 + \frac{Z_0}{Z_{\text{ant}}} \right) \right)} \quad (10)$$

$$V_{\text{rx}} = -2V_{\text{in,ant}} \frac{\frac{Z_0}{Z_{\text{ant}}} \left(\frac{Z_0}{R_{\text{sw}}} + \left(1 + \frac{Z_0}{Z_{\text{bal}}} \right) \right)}{\left(1 + \frac{Z_0}{Z_{\text{bal}}} \right) \left(2 + \frac{Z_0}{R_{\text{sw}}} \left(1 + \frac{Z_0}{Z_{\text{ant}}} \right) \right)}. \quad (11)$$

Fig. 6 shows the tradeoff between TX-BB isolation and ANT-RX loss by plotting V_1 using the above-mentioned equations for both TX and ANT excitations and different values of the balancing resistance ($Z_{\text{ant}} = 50\Omega$ and $R_{\text{sw}} = 3.5\Omega$). It can be seen that unlike the previous case, the ANT-to-gyrator loss increases with a lowering of the magnitude of Z_{bal} . Therefore, there exists a tradeoff between TX-BB isolation and ANT-BB loss using this balancing scheme.

The aforementioned approximate analysis captures the basics of how the balancing network functions in the circ.-RX, and shows how it can compensate for switch resistance parasitics. To verify this intuitive understanding for other types of parasitics, we have simulated our circ.-RX, along with an inductance–capacitance (LC) ladder-based balance network model as used in [10], also shown in Fig. 7. This impedance network can provide orthogonal impedance tunability just by varying the capacitor values. The inductors are fixed with a

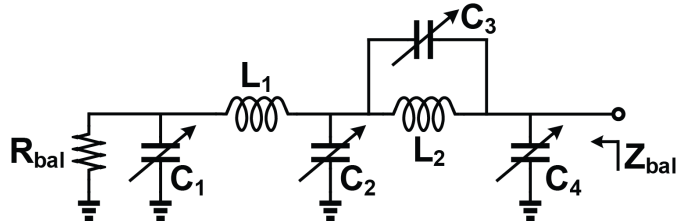


Fig. 7. Balance network structure used in simulations [10].

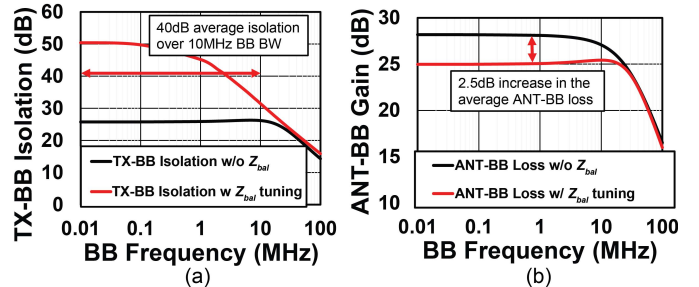


Fig. 8. Simulated (a) TX-BB isolation and (b) ANT-BB gain of the circ.-RX. Simulations are run on the extracted post-layout schematics of the circ.-RX, including wirebond inductance and package parasitics, with the LC ladder-based balance network (inductor $Q = 20$) model shown in Fig. 7.

Q of 20. The circ.-RX contains extracted layout parasitics, wirebond inductance and package parasitics. Fig. 8 shows the ANT-to-BB gain and the TX-to-BB isolation with and without the balance network, assuming 50Ω antenna impedance. As mentioned earlier, the balancing network is being used to compensate for layout parasitics, wirebond inductance, and package parasitics. More than 40-dB average isolation can be achieved over 20-MHz RF BW with a 2.5-dB degradation in the ANT-RX loss. In our implementation, discussed later in this paper, we have implemented a balance network consisting only of tunable capacitors and resistors, thanks to an Surface Mount Devices (SMD) Capacitor–Inductor–Capacitor (CLC)-based fixed ANT tuning network incorporated on the printed circuit board (PCB) performing a minor transformation (VSWR=1.2).

B. Noise Circulation

Here, we derive equations for the noise transfer function of the switch noise sources as well as the balance network. The circuit diagram for noise analysis is shown in Fig. 3(b) where the various noise sources are highlighted in red. The overall noise voltage at the gyrator is shown in (12), as shown at the top of the next page (assuming equal switch resistance on both sides of the gyrator). Where Γ_{bal} is the reflection coefficient of the balance network ($\Gamma_{\text{bal}} = (Z_{\text{bal}} - Z_0)/(Z_{\text{bal}} + Z_0)$), $\overline{V_{n,\text{ant}}} = 4\text{KT}Z_0$, $\overline{V_{n,i}} = 4\text{ KTR}_{\text{sw},i}$ ($i = 1, 2$), and $\overline{V_{n,\text{bal}}} = 4\text{ KT} \cdot \text{Re}(Z_{\text{bal}})$). This results in an equivalent NF as in (13).

It should be mentioned that (13), as shown at the top of the next page, only captures the noise of the circulator alone and does not include the noise of the following BB circuitry. In addition, the noise equations are all derived for $Z_{\text{ant}} = Z_0$, but can be modified to include the effect of varying antenna impedance. Since we are not working with large ANT variations in this paper, we have used the nominal antenna impedance for simplicity here.

$$\overline{V_1^2} = \overline{V_2^2} = \frac{1}{4} \overline{V_{n,\text{ant}}^2} \left(1 + \frac{\Gamma_{\text{bal}}}{1 + \frac{R_{\text{sw}}}{Z_0}} \right)^2 + \frac{1}{4} \overline{V_{n,1}^2} \left(1 - \frac{\Gamma_{\text{bal}}}{1 + \frac{R_{\text{sw}}}{Z_0}} \right)^2 + \frac{1}{4} \overline{V_{n,2}^2} \left(1 + \frac{\Gamma_{\text{bal}}}{1 + \frac{R_{\text{sw}}}{Z_0}} \right)^2 + \frac{1}{4} \overline{V_{n,\text{bal}}^2} (1 - \Gamma_{\text{bal}})^2 \quad (12)$$

$$F = 1 + \frac{R_{\text{sw}}}{Z_0} \left(\frac{1 + \frac{R_{\text{sw}}}{Z_0} - \Gamma_{\text{bal}}}{1 + \frac{R_{\text{sw}}}{Z_0} + \Gamma_{\text{bal}}} \right)^2 + \frac{R_{\text{sw}}}{Z_0} + \frac{\text{Re}(Z_{\text{bal}})}{Z_0} \left(\frac{(1 + \frac{R_{\text{sw}}}{Z_0})(1 - \Gamma_{\text{bal}})}{1 + \frac{R_{\text{sw}}}{Z_0} + \Gamma_{\text{bal}}} \right)^2. \quad (13)$$

$$\overline{V_{\text{ant}}^2} = \left(\frac{1}{1 + \frac{R_{\text{sw}}}{Z_0}} \right)^2 \left(\overline{V_{n,\text{ant}}^2} + \overline{V_{n,1}^2} + \overline{V_{n,2}^2} \right) \quad (14)$$

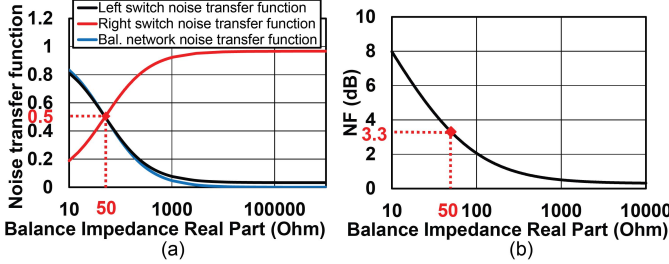


Fig. 9. (a) Noise transfer functions based on (12). (b) Theoretical NF of the circ.-RX in the presence of the balance network.

From these equations, it can be seen that the noise of the left-hand side switches contributes differently to the noise voltage at the gyrator than the noise from the antenna and the right-hand side switches. Assuming that R_{sw} is relatively small compared to Z_0 , it can be seen from (12) that the noise from the left-hand side switches vanishes at the gyrator node when there is no balance network. In the presence of the balance network, the noise transfer functions from the switches depend on the network's reflection coefficient. In addition, (14), as shown at the top of this page, shows how the noise from each of the noise sources appears at the ANT port. The noise of each of the switch resistances contribute equally to the overall noise at the ANT port and have a similar transfer function as the antenna impedance noise itself. Interestingly, the noise from the balance network does not appear on the ANT port. Fig. 9 shows the noise transfer functions to the BB node and the NF calculated earlier as a function of the balance network impedance for $R_{\text{sw}} = 3.5 \Omega$ (no other post-layout parasitics included). It should be mentioned that this NF plot is the worst case scenario, assuming that the balance network is completely resistive. As the balance network impedance becomes smaller, the noise contribution from the left-hand side switches and the balance network increases. For the optimal isolation ($Z_{\text{bal}} = 50 \Omega$, as calculated earlier), the NF degrades by about 3 dB. This shows the tradeoff between the TX-to-BB isolation and RX NF. Fig. 10(a) shows the NF simulations of the circ.-RX for $Z_{\text{ant}} = 50 \Omega$ with and without the balance network compensating for post-layout and package parasitics. The overall NF is degraded by around 2.5 to 4 dB. Our measured NF is higher due to the additional noise contributions from the BB amplifiers and the clock circuitry.

Clock phase noise can degrade the NF of the circulator [8] if the clock path is not properly designed. However a systematic design of the clock path eliminates the effect

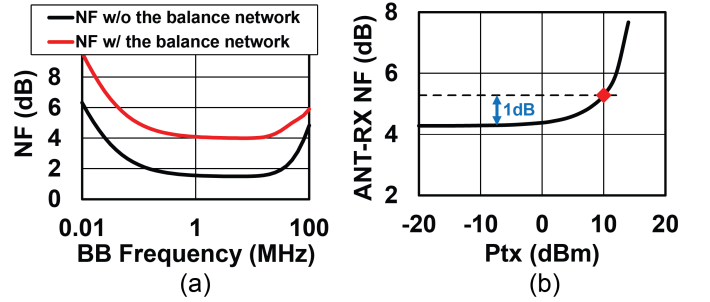


Fig. 10. (a) Simulated NF of the circ.-RX with and without the balance network optimized for 40-dB average isolation. (b) Simulated increase in the NF (average across 10 KHz–10 MHz) of the circ.-RX in the presence of a large TX signal (including the balance network optimized for 40-dB average isolation). The balance network settings are similar to those of the simulation results shown in Fig. 8.

of phase noise on passive commutation-based circulators' performance [31], [35]. Since circulators are intended to be used in simultaneous transmit and receive (STAR) applications, it is important to also consider ANT-RX NF in the presence of a powerful TX signal. In such a scenario, phase noise will produce a reciprocal mixing like effect with the TX signal. The simulated circ.-RX average NF in the presence of a large TX excitation and including the entire clock path implemented in this paper is plotted in Fig. 10(b). The circ.-RX NF degrades by 1 dB for +10 dBm of TX power. While it is clear that such a reciprocal mixing like effect is not severe for the power levels being considered in this paper, a theoretical treatment of this phenomenon, as has recently been done for N-path filters in [41], is an interesting topic for future research.

IV. IMPLEMENTATION

The block diagram and schematic of the 65-nm CMOS FD circ.-RX is shown in Fig. 11.

A. Integrated Circulator

The circulator was designed for tunable operation around 750 MHz in 65-nm CMOS technology. The $3\lambda/4$ line is miniaturized using three CLC sections implemented with on-chip MiM capacitors and off-chip air-core 8.9-nH inductors (0806SQ from Coilcraft, $Q_L > 100$). N-path filters/passive-mixers has been demonstrated at frequencies up to ~ 2 GHz [37] at 65-nm CMOS. The N-path-filter-based circulator can also be designed across this frequency range. We have designed our prototype for a 750-MHz center

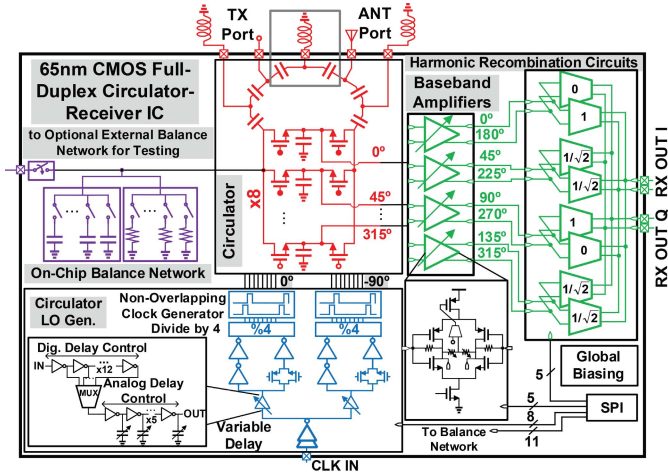


Fig. 11. Block diagram and schematic of the implemented 65-nm CMOS FD circ.-RX with integrated circulator and balancing impedance.

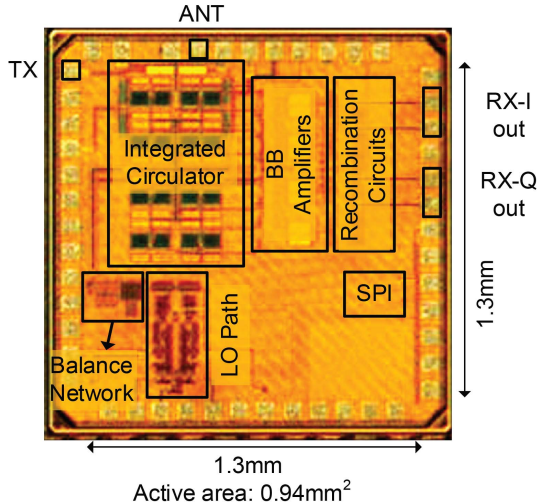


Fig. 12. Chip microphotograph of the 65-nm CMOS FD circ.-RX.

frequency and for 20-MHz operating BW considering the tradeoff between the complexity of the design of the clock-path and the size of the passive components. The N-path filter uses eight-paths to increase the ANT-RX BB recombination gain and achieve harmonic cancellation for the 3rd and 5th harmonics. The capacitance of each path is 16 pF. Switch resistance for each of the 16 transistors is around $3.5\ \Omega$. The sources/drains of switches are biased at 1.2 V and are DC coupled to the BB amplifiers (which run off a 2.4-V supply as is discussed later). The gates of the switches are AC coupled to the buffers and are biased at 1.35 V (dc level of a 12.5% pulse swinging from 1.2–2.4 V). The balance network is designed using a parallel resistive bank (6 bits) and a parallel capacitive bank (5 bits). More complex balance networks as demonstrated in [10] can be used to increase the range of balancing that can be performed. An input clock at four times the operating frequency provides eight output phases in a Johnson-counter-based divide-by-4 block. Clock phase-shifting is performed for one set of switches prior to division using multiplexed digital delay cells with analog varactor-based fine-tuning to cover a range of -76° to 78° around the nominal phase setting at 750 MHz based on schematic-level simulations at the typical corner. Simulations also reveal that in the worst

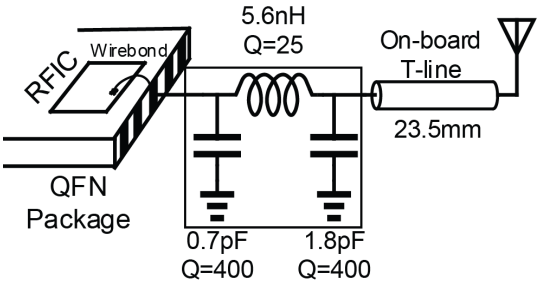


Fig. 13. SMD CLC-based ANT matching network used on the PCB to compensate for parasitics and achieve a reasonable nominal TX-to-RX isolation.

case (slow–slow corner) the clock path degrades the NF by about 0.25 dB. The post-layout simulated TX-ANT IIP3 is more than +30 dBm. The limiting factor in the maximum power that can be handled at the TX port in the circ.-RX structure is the ANT-BB gain/NF compression, which was shown previously in Fig. 10(b) (~ 10 dBm), rather than the P1dB of the TX-ANT path (~ 20 dBm). Further improvements in the TX-ANT IIP3 and the power handling can be achieved by taking advantage of Silicon-On-Insulator (SOI) CMOS process nodes with higher voltage handling as has been done in [35] using 180-nm SOI CMOS.

B. Integrated Receiver

The BB circuitry consists of a BB amplification stage and harmonic recombination circuitry. All the BB circuitry use thick-oxide devices and run off a 2.4-V supply to increase the power-handling of the circ.-RX. Four differential BB amplifiers are implemented, each using an inverter with large resistive feedback for self biasing and a common mode feedback circuit. A 5-bit variable resistor is added at the output to control the gain and BW.

Since the circulator is based on an eight-path filter, the BB signals have to be recombined to provide differential I/Q outputs. The outputs of the BB amplifiers are connected to the harmonic-recombination variable-gain G_m cells. The G_m cells are implemented as open-drain differential pairs with switchable devices for 5-bit variable gain. Note that the variable-gain control is common for all the G_m cells, and therefore, is not intended for harmonic rejection calibration. The differential outputs of the G_m cells are connected to off-chip baluns for testing. The $I+/-$ outputs are created by combining the differential $0/180^\circ$ phases with a weight of 1, $45/225^\circ$ phases with a weight of $\sqrt{2}/2$ and $135/315^\circ$ phases with a weight of $-\sqrt{2}/2$. Similarly, the $Q+/-$ outputs are generated by assigning a weight of 1 to the $90/270^\circ$ phases, and $\sqrt{2}/2$ weights to $45/225^\circ$ and $135/315^\circ$. This weighting cancels harmonics of the following orders: 3rd and 5th, 11th and 13th, and so on [37]. Similar to prior work, the harmonic rejection is limited to the precision of the $\sqrt{2}/2$ implementation and the mismatch between the devices. In this paper, this scaling factor has been incorporated into the relative width of the NMOS devices in the G_m cells. The overall harmonic rejection of the circ.-RX is expected to be more, due to the band-limited nature of the circulator transmission lines implemented in this paper.

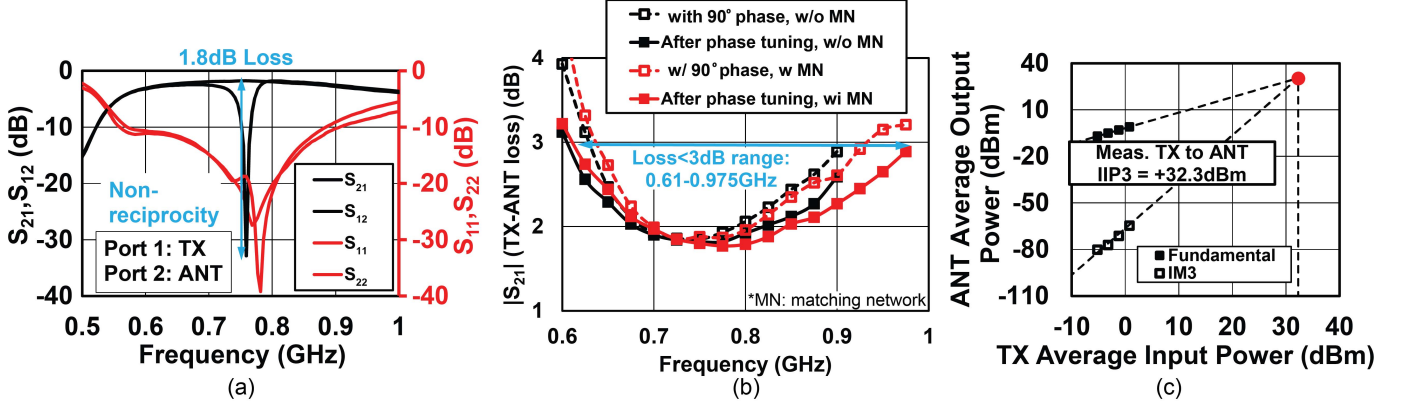


Fig. 14. (a) Circulator TX-to-ANT S-parameter measurements for 750-MHz clock frequency. (b) Measured TX-to-ANT loss at the center frequency as the clock frequency is tuned. Phase tuning is used at each frequency to ensure minimum loss. The black or red curves are without or with the SMD-based ANT matching network. (c) Measured IB TX-to-ANT IIP3.

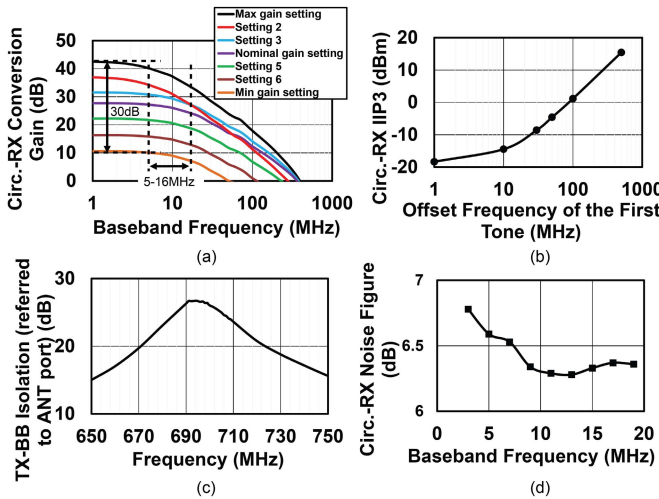


Fig. 15. Measured circ.-RX. (a) Conversion gain. (b) IIP3. (c) Small-signal TX-to-BB isolation for -40 -dB TX power. (d) NF. The balance network is not engaged in these measurements.

V. MEASUREMENT RESULTS

The chip microphotograph of the 65-nm CMOS circ.-RX is shown in Fig. 12. It has an active area of 0.94 mm^2 and is mounted in a 40-pin Quad-Flat No-leads (QFN) package. An SMD CLC-based fixed ANT tuning network as shown in Fig. 13 has been incorporated on the PCB performing a minor transformation ($\text{VSWR}=1.2$) to compensate for QFN parasitics and achieve a reasonable nominal TX-to-BB isolation when the balance network is off.

A. Integrated Circulator

The measured two-port TX-to-ANT S-parameters of the circulator for a clock frequency of 750 MHz are shown in Fig. 14(a). Note that the RX is not available as a separate RF port, and hence the circulator's ANT-to-RX and TX-to-RX performance cannot be measured directly using S-parameters. These performance metrics of the circulator are a part of the circ.-RX measurements reported in Section V-B. The minimum measured TX-to-ANT loss is 1.8 dB with only 0.1-dB degradation in a 100-MHz BW around the center frequency. Both the TX and ANT ports are well matched across a 300-MHz BW. Fig. 14(b) shows the TX-to-ANT loss at the center frequency as clock frequency is tuned.

For each clock frequency, phase shift tuning between the clocks on either side is used to minimize the losses. At each clock frequency, a search around the default setting (calculated based on the phase shift of the t-line sections) is carried out to determine the lowest TX-ANT loss, while keeping the baseline isolation above 15 dB. The off-chip SMD-based matching network also improves the frequency range across which the S_{21} remains below 3 dB by making the ANT impedance closer to the nominal 50Ω . Less than 3-dB loss is maintained over 610–975 MHz by using the off-chip matching network. The measured circulator inband (IB) TX-to-ANT IIP3 is $+32.3$ dBm as shown in Fig. 14(c). This is higher compared to the implementation in [8] due to the lower R_{sw} and the higher initial TX-to-RX isolation due to the SMD-based matching network.

B. Circ.-RX Measurements Without the Balance Network

The circ.-RX operates over the frequency range of the on-chip integrated circulator, namely, 610–975 MHz, with a measured variable gain of 10–42 dB and a nominal gain of 28 dB. The RF BW of the circulator varies over 10–32 MHz as the gain is varied [Fig. 15(a)]. The measured IB IIP3 of the circ.-RX is -18.4 dBm at the nominal gain setting, and the measured out-of-band IIP3 is $+15.4$ dBm at a 500-MHz offset frequency as shown in Fig. 15(b). Our measured Out-Of-Band (OOB) IIP3 value is similar to that of mixer-first RXs [17], [37], and can be improved to reach higher values with the use of more stages of low-pass filtering through the RX chain. The measured TX-to-BB isolation referred to the ANT port is better than 20 dB over more than 50-MHz BW (6.7% fractional BW) for a -40 -dB TX excitation after optimizing the on-board matching network. A RX NF of 6.3 dB is measured, and is comparable to or better than that of mixer-first RXs used for FD [17], [19] thanks to the relaxed RX 50Ω matching requirements and the effect of noise circulation. It should be emphasized that our reported NF encompasses both the RX and an on-chip shared-ANT interface.

C. Circ.-RX Measurements With the Balance Network

Engaging and optimizing the balance network dramatically improves the isolation for both the small-signal and large-

TABLE I
PERFORMANCE SUMMARY AND COMPARISON WITH STATE-OF-THE-ART FD RXS.

	JSSC 2015 [19]	JSSC 2017 [14]	RFIC 2017 [15]	JSSC 2015 [17]	JSSC 2017 [8]	This work
RX metrics	Architecture	Mixer-first RX with SI-cancelling VM-downmixer	Dual path + adaptive filter	Electrical-balanced duplexer + mixer-first RX	Mixer-first TRX with active BB duplexing	RX with integrated magnetic-free N-path-filter-based circulator-receiver with on-chip balance network
	RX Frequency Range	0.15-3.5GHz	1.7-2.2GHz	1-2GHz	0.1-1.5GHz	0.61-0.975GHz
	Gain	24dB	20-36dB	35dB	53dB	42dB
	Noise Figure	6.3dB	4dB	3.8dB ² (6dB ³)	5-8dB	8.4dB
	OOB IIP3	+22.0dBm	N/R	+25dBm	+22.5dBm	+19dBm
	IB IIP3	+9 / +19dBm at 24dB gain (Neg. conductance off/on)	-5dBm at 30dB gain	+1dBm ²	-38.7dBm at 53dB gain	-33dBm at 42dB gain
	Integrated Antenna Interface	No	No	Yes (electrical-balanced duplexer)	Yes (baseband duplexing LNA)	Yes (magnetic-free non-reciprocal circulator)
	Integrated SI Suppression Domains	Analog BB	RF + Analog BB	RF	Analog BB	RF + Analog BB
	Amount of Integrated SI Suppression	21dB SIC across ~16MHz BW	50dB SIC across 42MHz BW	64dB across 20MHz BW	33dB across 300kHz TX BB BW	42dB SIC across 12MHz BW
	Effective IIP3 with respect to RX/ANT Input	+21.5dBm at 24dB gain	+17dBm at 30dB gain	N/A	N/A	N/A
Full-Duplex Metrics	Effective IIP3 with respect to TX Port	N/A	N/A	N/R	~0dBm at 43/53dB gain ⁴	+1dBm at 42dB gain
	Overall TX Port Power Handling	N/A	25dBm (prior to 30-35dB off-chip isolation)	+5dBm (w/o a circulator)	-17.3dBm ⁵	-7dBm ⁵
	NF in Full-Duplex Mode	10.3-12.3dB ¹	5.55dB	7-15.4dB in FDD mode	-10dB ^{6,7}	10.9dB ⁷
	Overall SI Suppression	46dB (incl. 25dB isolation from antenna pair)	80-85dB	89-94dB (incl. digital SIC) in FDD mode	33dB	85dB (incl. digital SIC)
	RX Power	23-56mW	33.5mW	64mW	43-56mW (incl. TX)	100mW
	Antenna Interface Power	N/A	N/A	N/A	Incl. in RX power	59mW (at 0.7GHz)
	Technology	65nm CMOS	40nm CMOS	65nm CMOS	65nm CMOS	65nm CMOS
	Active Area	2mm ²	3.5mm ²	0.33mm ² ²	1.5mm ²	1.4mm ²
Resources						72mW (BB amplifiers: 40mW Recombination circuitry: 32mW)
						36mW (at 0.7GHz)

1. Across VM settings. 2. From S. Ramakrishnan's PhD thesis. 3. Including cancellation network loss 4. From Fig. 31(a) in the paper.

5. Limited by ~1dB gain compression induced in the receive signal. 6. at -17.3dBm TX power. 7. Includes antenna interface.

N/A: Not Applicable N/R: Not Reported

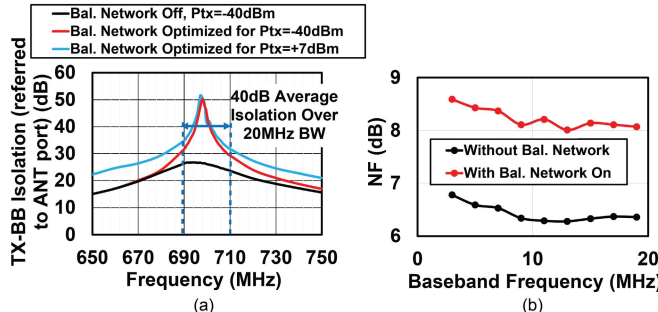


Fig. 16. (a) Measured small and large signal TX-to-BB isolation after engaging the balance network. The balance network is reconfigured to maintain isolation for each TX power level. (b) Measured impact of the balance network on RX NF in the FD mode.

signal TX excitations [Fig. 16(a)]. The average large-signal isolation for a TX power of +7 dBm improves to 40 dB over 20-MHz BW. At the optimized balance network setting, the NF degrades by 1.7 to 8 dB [Fig. 16(b)]. Enabling the balance network also enhances the TX power for 1-dB gain compression of a weak desired signal from 0 to +8 dBm as shown in Fig. 17. Fig. 18(b) depicts a two-tone TX test, tracking the TX main SI and its IM3 distortion at the RX output. We have also implemented digital SIC in MATLAB after capturing the

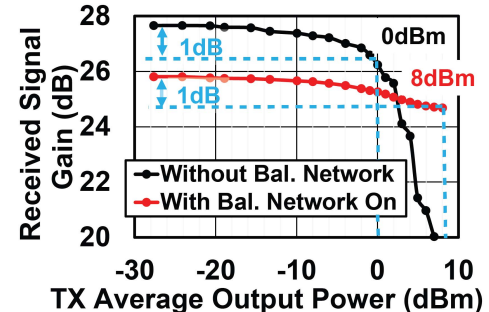


Fig. 17. Measured ANT-to-RX-BB gain compression of a weak desired signal with and without balance network tuning versus varying TX output power level.

BB signals using an oscilloscope (a 12b quantizer). The digital SIC cancels not only the main SI but also the IM3 distortion generated from the SI [Fig. 18(a)]. The total SIC for the main TX tones and TX IM3 tones are 86 and 80 dB at +8 dBm average TX power, respectively. The effective noise floor after digital SIC is -73 dBm. As mentioned earlier, providing an additional 20-dB BB SIC, as shown before in [8], would result in an overall noise floor of -93 dBm and enable a link range of 100 m at the operation frequency.

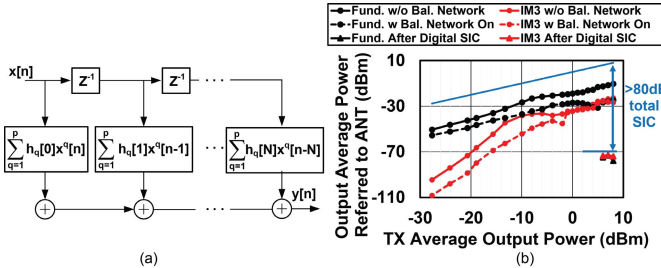


Fig. 18. (a) Nonlinear tapped delay line used for digital SIC. (b) Measured two-tone TX test tracking the SI and its IM3 distortion at the RX BB output with SI suppression across antenna and digital domains.

D. Comparison to the State of the Art

Table I compares this paper to prior integrated FD RXs. This paper has the highest TX power handling and isolation BW and the lowest NF among FD RXs with an integrated antenna interface. It also provides the benefit of embedding a balancing impedance to tune TX-to-RX isolation for minor antenna VSWRs. When compared with our prior work in [8], this paper has lower power consumption, better NF, higher tuning range, wider isolation BW, and higher effective IIP3 with respect to the TX port (and hence, higher TX power handling).

VI. FD DEMONSTRATION

To demonstrate the effectiveness of the circ.-RX architecture, a demonstration has been carried out in which a powerful modulated transmitted signal is canceled while a weak continuous-wave desired signal is received from the antenna port.

An orthogonal frequency-division multiplexing (OFDM)-like BB signal is generated at a sampling rate of 160 MSa/s, and it consists of 10 sub-carriers each with a BW of 0.4 MHz occupying a total BW of 5 MHz (1-MHz dc has been omitted due to implementation limitations related to the high-pass cutoff frequency of the off-chip BB baluns). The OFDM-like signal is pulse shaped with square-root-raised-cosine (SRRC) filter with a roll-off factor of $\beta = 0.22$. The total length of the OFDM-like signal is chosen to be 50 000 samples with an extra 2000 samples to sync the received sequence to the transmitted signal. Fig. 19(a) shows a simulated frequency-domain representation of the generated pulse-shaped OFDM-like signal used in this demonstration.

Fig. 19(b) shows the demonstration setup. The TX is built using off-the-shelf components as follows. An I/Q quadrature modulator (Texas Instruments TRF370417 EVM module) is followed by a Mini-Circuits ZHL-42 power amplifier. The BB OFDM-like signal is generated in MATLAB, and is fed to an Agilent 33500B arbitrary waveform generator (AWG), which is connected through a balun to the quadrature modulator. The clocks of the radio-frequency integrated circuits (RFIC) circ.-RX and the TX are shared from a signal source running at $4\times$ the frequency of operation (2.8 GHz) to lower the effects of uncorrelated phase noise [42]–[44]. A separate frequency-division module is used to divide down the clock to 700 MHz for the TX.

First, to verify successful digital SIC of modulated signals, a 0-dBm average power TX signal is applied to the TX port

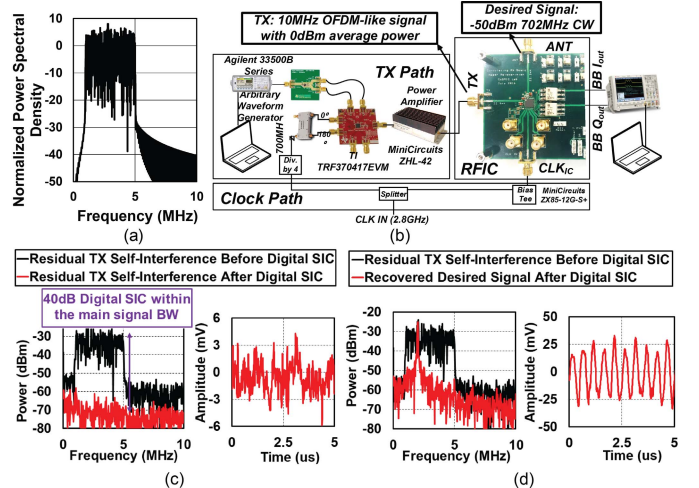


Fig. 19. (a) Simulated BB frequency domain representation of the generated pulse-shaped OFDM-like signal used in the FD demo. (b) FD demonstration setup. FD demo results: a –50-dBm weak desired signal is received while transmitting a 0-dBm average power OFDM-like signal. Power spectral density and time-domain representation of the RX BB output before and after digital SIC are shown (c) without the desired ANT signal and (d) with the desired ANT signal. The single tone ANT signal is recovered after digital SIC.

and the residual BB leakage is captured on the oscilloscope. In our digital SIC, nonlinear terms up to seventh order are considered, with a delay spread length of 45 samples, resulting in 315 total unknown canceller coefficients. An initial portion of the captured data (about $80\mu s$) is used to train the canceller coefficients. Fig. 19(c) and (d) shows the power spectral density at the RX BB output before and after the digital SIC of the TX leakage. 38-dB digital SIC and about 70-dB overall SIC has been achieved. In addition, a –50-dBm weak continuous-wave desired signal at 702 MHz is applied to the ANT port, and is initially buried under the TX leakage at the RX BB before digital SIC. Once digital SIC is engaged, the desired signal is recovered, as can be seen in the time-domain and frequency-domain signal representations shown in Fig. 19(d).

VII. CONCLUSION

We have demonstrated a magnetic-free non-reciprocal N-path-filter-based circ.-RX architecture for FD wireless. The innovations include merging the commutation of the circulator with the down-conversion mixer to eliminate the RX LNA and mixer, incorporation of an additional balancing impedance for fine-tuning of the TX-to-RX isolation, and noise circulation of one set of commutating switches. A prototype 65-nm CMOS 750-MHz circ.-RX is presented, which achieves 40-dB SIC across 20-MHz BW with lower NF and power consumption than prior works. In conjunction with digital SIC, the FD circ.-RX demonstrates 80-dB overall SI suppression for up to +8-dBm TX average output power.

Future research directions include further improvements of the circulator's linearity performance and the TX power handling and improved balancing schemes to account for a wider range of antenna impedance mismatches. At the system

level, extending the research on integrated FD RXs to FD multi-antenna systems is of significant interest.

REFERENCES

- [1] I. Chih-Lin, C. Rowell, S. Han, Z. Xu, G. Li, and Z. Pan, "Toward green and soft: A 5G perspective," *IEEE Commun. Mag.*, vol. 52, no. 2, pp. 66–73, Feb. 2014.
- [2] S. Chen and J. Zhao, "The requirements, challenges, and technologies for 5G of terrestrial mobile telecommunication," *IEEE Commun. Mag.*, vol. 52, no. 5, pp. 36–43, May 2014.
- [3] D. Bharadia, E. McMillin, and S. Katti, "Full duplex radios," in *Proc. ACM SIGCOMM Conf. (SIGCOMM)*, 2013, pp. 375–386.
- [4] A. Sabharwal, P. Schniter, D. Guo, D. W. Bliss, S. Rangarajan, and R. Wichman, "In-band full-duplex wireless: Challenges and opportunities," *IEEE J. Sel. Areas Commun.*, vol. 32, no. 9, pp. 1637–1652, Sep. 2014.
- [5] D. Kim, H. Lee, and D. Hong, "A survey of in-band full-duplex transmission: From the perspective of PHY and MAC layers," *IEEE Commun. Surveys Tuts.*, vol. 17, no. 4, pp. 2017–2046, 4th Quart., 2015.
- [6] J. Zhou *et al.*, "Integrated full duplex radios," *IEEE Commun. Mag.*, vol. 55, no. 4, pp. 142–151, Apr. 2017.
- [7] N. Reiskarimian and H. Krishnaswamy, "Magnetic-free non-reciprocity based on staggered commutation," *Nature Commun.*, vol. 7, no. 4, Apr. 2016, Art. no. 11217.
- [8] N. Reiskarimian, J. Zhou, and H. Krishnaswamy, "A CMOS passive LPTV nonmagnetic circulator and its application in a full-duplex receiver," *IEEE J. Solid-State Circuits*, vol. 52, no. 5, pp. 1358–1372, May 2017.
- [9] M. Elkholly, M. Mikhemar, H. Darabi, and K. Entesari, "Low-loss integrated passive CMOS electrical balance duplexer with single-ended LNA," *IEEE Trans. Microw. Theory Techn.*, vol. 64, no. 5, pp. 1544–1559, May 2016.
- [10] B. van Liempd *et al.*, "A +70-dBm IIP3 electrical-balance duplexer for highly integrated tunable front-ends," *IEEE Trans. Microw. Theory Techn.*, vol. 64, no. 12, pp. 4274–4286, Dec. 2016.
- [11] S. H. Abdelhalem *et al.*, "Tunable CMOS integrated duplexer with antenna impedance tracking and high isolation in the transmit and receive bands," *IEEE Trans. Microw. Theory Techn.*, vol. 62, no. 9, pp. 2092–2104, Sep. 2014.
- [12] T. Dinc, A. Chakrabarti, and H. Krishnaswamy, "A 60 GHz CMOS full-duplex transceiver and link with polarization-based antenna and RF cancellation," *IEEE J. Solid-State Circuits*, vol. 51, no. 5, pp. 1125–1140, May 2016.
- [13] T. Dinc and H. Krishnaswamy, "A T/R antenna pair with polarization-based reconfigurable wideband self-interference cancellation for simultaneous transmit and receive," in *IEEE MTT-S Int. Microw. Symp. Dig.*, May 2015, pp. 1–4.
- [14] T. Zhang, C. Su, A. Najafi, and J. C. Rudell, "Wideband dual-injection path self-interference cancellation architecture for full-duplex transceivers," *IEEE J. Solid-State Circuits*, to be published.
- [15] S. Ramakrishnan, L. Calderin, A. Niknejad, and B. Nikolic, "An FD/FDD transceiver with RX band thermal, quantization, and phase noise rejection and >64 dB TX signal cancellation," in *Proc. IEEE Radio Freq. Integr. Circuits Symp. (RFIC)*, Jun. 2017, pp. 352–355.
- [16] E. Kargaran, S. Tijani, G. Pini, D. Manstretta, and R. Castello, "Low power wideband receiver with RF self-interference cancellation for full-duplex and FDD wireless diversity," in *Proc. IEEE Radio Freq. Integr. Circuits Symp. (RFIC)*, Jun. 2017, pp. 348–351.
- [17] D. Yang, H. Yüksel, and A. Molnar, "A wideband highly integrated and widely tunable transceiver for in-band full-duplex communication," *IEEE J. Solid-State Circuits*, vol. 50, no. 5, pp. 1189–1202, May 2015.
- [18] J. Zhou, T.-H. Chuang, T. Dinc, and H. Krishnaswamy, "Integrated wideband self-interference cancellation in the RF domain for FDD and full-duplex wireless," *IEEE J. Solid-State Circuits*, vol. 50, no. 12, pp. 3015–3031, Dec. 2015.
- [19] D.-J. van den Broek, E. A. M. Klumperink, and B. Nauta, "An in-band full-duplex radio receiver with a passive vector modulator downmixer for self-interference cancellation," *IEEE J. Solid-State Circuits*, vol. 50, no. 12, pp. 3003–3014, Dec. 2015.
- [20] J. Zhou, A. Chakrabarti, P. R. Kinget, and H. Krishnaswamy, "Low-noise active cancellation of transmitter leakage and transmitter noise in broadband wireless receivers for FDD/co-existence," *IEEE J. Solid-State Circuits*, vol. 49, no. 12, pp. 3046–3062, Dec. 2014.
- [21] D. Korpi *et al.*, "Full-duplex mobile device: Pushing the limits," *IEEE Commun. Mag.*, vol. 54, no. 9, pp. 80–87, Sep. 2016.
- [22] X. Du, J. Tadrous, and A. Sabharwal, "Sequential beamforming for multiuser MIMO with full-duplex training," *IEEE Trans. Wireless Commun.*, vol. 15, no. 12, pp. 8551–8564, Dec. 2016.
- [23] SKYFR-000709: 2110–2170 MHz Single Junction Robust Lead Circulator, Skyworks Solutions, Woburn, MA, USA, May 2013.
- [24] S. A. Ayati, D. Mandal, B. Bakkaloglu, and S. Kiaei, "Adaptive integrated CMOS circulator," in *Proc. IEEE Radio Freq. Integr. Circuits Symp. (RFIC)*, May 2016, pp. 146–149.
- [25] B. van Liempd, A. Visweswaran, S. Arimi, S. Hitomi, P. Wambacq, and J. Crainckx, "Adaptive RF front-ends using electrical-balance duplexers and tuned SAW resonators," *IEEE Trans. Microw. Theory Techn.*, vol. 65, no. 11, pp. 4621–4628, Nov. 2017.
- [26] A. K. Kamal, "A parametric device as a nonreciprocal element," *Proc. IRE*, vol. 48, no. 8, pp. 1424–1430, Aug. 1960.
- [27] H. E. Brenner, "A unilateral parametric amplifier," *IEEE Trans. Microw. Theory Techn.*, vol. MTT-15, no. 5, pp. 301–306, May 1967.
- [28] A. Kord, D. L. Sounas, and A. Alù, "Magnet-less circulators based on spatiotemporal modulation of bandstop filters in a delta topology," *IEEE Trans. Microw. Theory Techn.*, vol. 66, no. 2, pp. 911–926, Feb. 2017.
- [29] N. A. Estep, D. L. Sounas, and A. Alù, "Magnetless microwave circulators based on spatiotemporally modulated rings of coupled resonators," *IEEE Trans. Microw. Theory Techn.*, vol. 64, no. 2, pp. 502–518, Feb. 2016.
- [30] S. Qin, Q. Xu, and Y. E. Wang, "Nonreciprocal components with distributedly modulated capacitors," *IEEE Trans. Microw. Theory Techn.*, vol. 62, no. 10, pp. 2260–2272, Oct. 2014.
- [31] T. Dinc and H. Krishnaswamy, "A 28 GHz magnetic-free non-reciprocal passive CMOS circulator based on spatio-temporal conductance modulation," in *IEEE Int. Solid-State Circuits Conf. (ISSCC) Dig. Tech. Papers*, Feb. 2017, pp. 294–295.
- [32] T. Dinc, M. Tymchenko, A. Nagulu, D. Sounas, A. Alù, and H. Krishnaswamy, "Synchronized conductivity modulation to realize broadband lossless magnetic-free non-reciprocity," *Nature Commun.*, vol. 8, no. 10, Oct. 2017, Art. no. 795.
- [33] M. M. Biedka, R. Zhu, Q. M. Xu, and Y. E. Wang, "Simultaneous transmission and receive (STAR) from DC to RF," in *IEEE MTT-S Int. Microw. Symp. Dig.*, Jun. 2017, pp. 1774–1777.
- [34] J. Zhou, N. Reiskarimian, and H. Krishnaswamy, "Receiver with integrated magnetic-free N-path-filter-based non-reciprocal circulator and baseband self-interference cancellation for full-duplex wireless," in *IEEE Int. Solid-State Circuits Conf. (ISSCC) Dig. Tech. Papers*, Jan. 2016, pp. 178–180.
- [35] A. Nagulu, A. Alù, and H. Krishnaswamy, "Fully-integrated non-magnetic 180 nm SOI circulator with >1W P1dB, >+50 dBm IIP3 and high isolation across 1.85 VSWR," in *Proc. IEEE Radio Freq. Integr. Circuits Symp. (RFIC)*, 2018.
- [36] N. Reiskarimian, M. B. Dastjerdi, J. Zhou, and H. Krishnaswamy, "Highly-linear integrated magnetic-free circulator-receiver for full-duplex wireless," in *IEEE Int. Solid-State Circuits Conf. (ISSCC) Dig. Tech. Papers*, Feb. 2017, pp. 316–317.
- [37] C. Andrews and A. C. Molnar, "A passive mixer-first receiver with digitally controlled and widely tunable RF interface," *IEEE J. Solid-State Circuits*, vol. 45, no. 12, pp. 2696–2708, Dec. 2010.
- [38] N. Reiskarimian, J. Zhou, T.-H. Chuang, and H. Krishnaswamy, "Analysis and design of two-port N-path bandpass filters with embedded phase shifting," *IEEE Trans. Circuits Syst. II, Exp. Briefs*, vol. 63, no. 8, pp. 728–732, Aug. 2016.
- [39] B. Razavi, *RF Microelectronics*. Englewood Cliffs, NJ, USA: Prentice-Hall, 2012.
- [40] D. Yang, C. Andrews, and A. Molnar, "Optimized design of n-phase passive mixer-first receivers in wideband operation," *IEEE Trans. Circuits Syst. I, Reg. Papers*, vol. 62, no. 11, pp. 2759–2770, Nov. 2015.
- [41] T. Tapen, Z. Boynton, H. Yüksel, A. Apsel, and A. Molnar, "The impact of lo phase noise in N-path filters," *IEEE Trans. Circuits Syst. I, Reg. Papers*, vol. 65, no. 5, pp. 1481–1494, May 2018.
- [42] J. Zhou and H. Krishnaswamy, "A system-level analysis of phase noise in full-duplex wireless transceivers," *IEEE Trans. Circuits Syst. II, Exp. Briefs*, to be published.
- [43] D. J. van den Broek, E. A. M. Klumperink, and B. Nauta, "A self-interference cancelling front-end for in-band full-duplex wireless and its phase noise performance," in *Proc. IEEE Radio Freq. Integr. Circuits Symp. (RFIC)*, May 2015, pp. 75–78.
- [44] A. Sahai, G. Patel, C. Dick, and A. Sabharwal, "On the impact of phase noise on active cancellation in wireless full-duplex," *IEEE Trans. Veh. Technol.*, vol. 62, no. 9, pp. 4494–4510, Nov. 2013.



Negar Reiskarimian (S'15) received the B.Sc. and M.Sc. degrees from the Sharif University of Technology, Tehran, Iran, in 2011 and 2013. She is currently pursuing the Ph.D. degree in electrical engineering with Columbia University, New York, NY, USA.

Her current research interests include integrated circuits and systems, applied electromagnetics, and nanophotonics, with a focus on theory, design and experimental validation of analog, radio-frequency, millimeter-Wave and optical integrated circuits, metamaterials and systems for a variety of applications, such as emerging wireless communications paradigms, Internet of Things, imaging, sensing, and opto/bio-electronics.

Ms. Reiskarimian was a recipient of the Marconi Society Paul Baran Young Scholar Award, the Qualcomm Innovation Fellowship, the IEEE Solid-State Circuits Society Predoctoral Achievement Award, the International Solid-States Circuits Conference Analog Devices Outstanding Student Designer Award, and the IEEE Microwave Theory and Techniques Society Graduate Fellowship. She was also featured in Forbes 30 under 30 list in 2018, and participated in Caltech's Young Investigator Lecture series in Engineering and Applied Sciences and Stanford's EECS Rising Star workshop.



Mahmood Baraani Dastjerdi (S'15) received the M.S. degree from the Sharif University of Technology, Tehran, Iran, in 2014. He is currently pursuing the Ph.D. degree in electrical engineering with Columbia University, New York, NY, USA.

His current research interests include the radio frequency (RF) circuits and systems.

Mr. Dastjerdi was a recipient of the 2018 Analog Devices Outstanding Student Designer Award.



Jin Zhou (S'11–M'17) received the B.S. degree in electronics science and technology from Wuhan University, Wuhan, China, in 2008, the M.S. degree in microelectronics from Fudan University, Shanghai, China, in 2011, and the Ph.D. degree in electrical engineering from Columbia University, New York, NY, USA, in 2017.

From 2011 to 2012, he was an RF Integrated Circuits Design Engineer with MediaTek, Singapore. In 2017, he joined the Department of Electrical and Computer Engineering with the University of Illinois at Urbana–Champaign, Urbana, IL, USA, as an Assistant Professor.

Dr. Zhou was a recipient of the 2015–2016 Qualcomm Innovation Fellowship, the 2015–2016 IEEE Solid-State Circuits Society (SSCS) Predoctoral Achievement Award, and the 2015–2016 Jury Award from the Department of Electrical Engineering, Columbia University for outstanding achievements in the areas of systems, communications, signal processing, or circuits.



Harish Krishnaswamy (S'03–M'09) received the B.Tech. degree in electrical engineering from IIT Madras, Chennai, India, in 2001, and the M.S. and Ph.D. degrees in electrical engineering from the University of Southern California (USC), Los Angeles, CA, USA, in 2003 and 2009, respectively.

In 2009, he joined the Electrical Engineering Department, Columbia University, New York, NY, USA, where he is currently an Associate Professor and the Director of the Columbia High-Speed and Millimeter-Wave IC Laboratory (CoSMIC). In 2017, he co-founded MixComm Inc., Chatham, NJ, USA, a venture-backed startup, to commercialize CoSMIC Laboratory's advanced wireless research. His current research interests include integrated devices, circuits, and systems for a variety of RF, mmWave, and sub-mmWave applications.

Dr. Krishnaswamy has been a member of the Technical Program Committee of several conferences, including the IEEE International Solid-State Circuits Conference since 2015 and the IEEE Radio Frequency Integrated Circuits Symposium since 2013. He is currently serving as a Distinguished Lecturer for the IEEE Solid-State Circuits Society and a member of the DARPA Microelectronics Exploratory Council. He was a recipient of the IEEE International Solid-State Circuits Conference Lewis Winner Award for Outstanding Paper in 2007, the Best Thesis in Experimental Research Award from the USC Viterbi School of Engineering in 2009, the Defense Advanced Research Projects Agency Young Faculty Award in 2011, the 2014 IBM Faculty Award, and the 2015 IEEE Radio Frequency Integrated Circuits Symposium Best Student Paper Award (First Place).